Electronic Supplementary Material (ESI) for Journal of Materials Chemistry A.

Supporting Information

Ruthenium-nickel-nickel hydroxide nanoparticles for room temperature catalytic hydrogenation

Lihua Zhu,*[ab] Shiyao Shan,[d] Valeri Petkov,[e] Weiwei Hu,[c] Anna Kroner,[f] Jinbao Zheng,[b] Changlin Yu,[a] Nuowei Zhang,[b] Yunhua Li,[b] Rafael Luque,*[bg] Chuan-Jian Zhong,[d] Hengqiang Ye,[c] Zhiqing Yang,*[c] and Bing H Chen*[b]

[a] School of Metallurgy and Chemical Engineering, Jiangxi University of Science and Technology, Ganzhou 341000, Jiang Xi, China

[b] Department of Chemical and Biochemical Engineering, National Engineering Laboratory for Green Productions of Alcohols-Ethers-Esters, College of Chemistry and Chemical Engineering, Xiamen University, Xiamen 361005, China

[c] Shenyang National Laboratory for Materials Science, Institute of Metal Research, Chinese Academy of Sciences, Shenyang 110016, China

[d] Department of Chemistry, State University of New York at Binghamton, Binghamton, New York 13902, United States

[e] Department of Physics, Central Michigan University, Mt. Pleasant, Michigan 48859, United States

[f] Diamond Light Source, Diamond House, Harwell Science and Innovation Campus, Chilton, Oxfordshire, OX11 0DE, United Kingdom

[g] Departamento de Química Orgánica, Universidad de Córdoba, Campus de Rabanales, Edificio Marie Curie (C-3), Ctra Nnal IV, Km 396, E14071, Córdoba, Spain

Corresponding Authors

lihuazhu@stu.xmu.edu.cn (L Zhu); q62alsor@uco.es (R Luque); yangzq@imr.ac.cn (Z Yang); chenbh@xmu.edu.cn (B H Chen).

1. Catalytic activity of the reported catalysts

As listed in Table S1, the Ru/Ni/Ni$(OH)_2$/C catalyst has excellent catalytic performance and high selectivity to decalin in naphthalene hydrogenation among a number of catalysts reported in literatures under similar reaction conditions. More importantly, to the best of our knowledge, the heterogeneous hydrogenation of naphthalene can be successfully conducted under unprecedentedly mild reaction conditions. The high catalytic activity of this catalyst is mainly attributed to the synergy effect of multiple catalytic sites (Ru, Ni and Ni$(OH)_2$).

Table S1: Catalytic performance of the catalysts for naphthalene hydrogenation in the reported literatures.

Ref	Catalyst	Solvent[a]	t (h)	P (H_2) (MPa)	T (°C)	TOF (h^{-1})	Selectivity	Yield[b]
1	Rh/AlO(OH)[1]	hexane	10	0.1	22	50	100%	100%[b]
2[c]	6%Pd/HY[2]	n-tridecane	0.1	10	200	-	100%	100%
3[d]	10%Ni/SBA-15[3]	n-dodecane	2	5	300	-	81.9%	81.9%
4[e]	Pd/Beta-H[4]	n-dodecane	1	0.28	340	-	31.7%	11.5%
5[f]	5%Rh/HSAG300[5]	scCO_2	-	18.0	40	3600~4200	-	3.2~9%
6[g]	$AlCl_3$+Pd/Al_2O_3[6]	-	1.0	1.0	30	-	0.1%	0.1%
7[h]	67%NiO-SiO_2-Al_2O_3[7]	toluene	-	1.0	200	-	-	12%
This work	Ru/Ni/Ni$(OH)_2$/C	cyclohexane	0.5	4.48	100	158.9	100%	100%
This work	Ru/Ni/Ni$(OH)_2$/C	cyclohexane	75	1.45	15	0.4	100%	100%

[a] The solvent was used to dissolve naphthalene;

[b] Yield to decalin;

[c] 0.4 g catalyst, 1.0 g (7.8 mmol) naphthalene dissolved in 4.0 g n-tridecane as reaction liquid, the conversion of naphthalene is 100%;

[d] 10.0 g of the solution of naphthalene in n-dodecane (5.0 wt%), the selectivity to tetralin is 18.1% and conversion of naphthalene is 100%, the used catalyst is 0.12 g;

[e] The selectivity to tetralin is 63.7% and conversion of naphthalene is 36.3%, the used catalyst is 0.33 g and naphthalene (5 g) was dissolved in dodecane (120 mL);

[f] The hydrogenation of naphthalene was performed in supercritical carbon dioxide (scCO$_2$), turnover frequency (TOF) values were also calculated on the assumption that number of adsorbed hydrogen atoms is the number of active sites, the selectivity to tetralin is 90~95%;

[g] Naphthalene: substrate (1 mmol) was dissolved in dichloromethane (2 mL), catalyst Pd/Al$_2$O$_3$ (5 mol%), AlCl$_3$ (10 mol% of naphthalene), the yield to tetralin is 99.9% and conversion of naphthalene is 100%;

[h] WHSV = 0.4 h^{-1}, naphthalene, Si/Al~11, reduction temperature of the catalyst = 300 °C, H$_2$ = 19 ml/min, The yield to tetralin is 76% and conversion of naphthalene is 88%.

2. TEM images and NPs size distribution for the Ni/Ni(OH)$_2$/C, Ru/C and Ru/Ni/Ni(OH)$_2$/C samples

Typical transmission electron microscopy (TEM) images and the corresponding NPs size distributions for the Ni/Ni(OH)$_2$/C, Ru/C and Ru/Ni/Ni(OH)$_2$/C samples are displayed in Fig. S1. The average size of Ni/Ni(OH)$_2$, Ru and Ru/Ni/Ni(OH)$_2$ NPs in the Ni/Ni(OH)$_2$/C, Ru/C and Ru/Ni/Ni(OH)$_2$/C samples is about 7.87 nm, 4.46 nm and 6.92 nm, respectively. The NPs in these samples are with narrow size distributions.

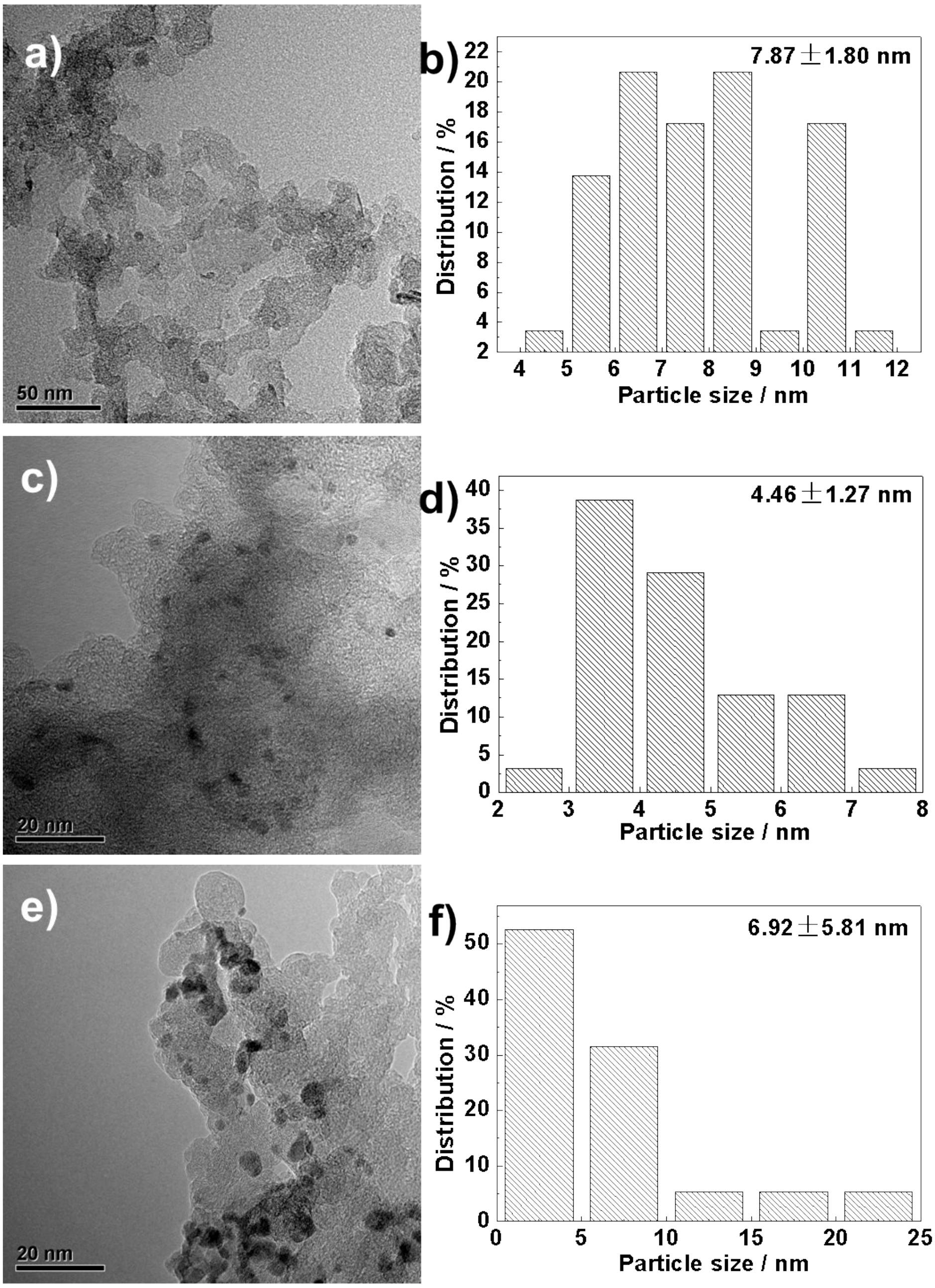

Fig. S1. TEM image and NPs size distribution for the (a, b) $Ni/Ni(OH)_2/C$, (c, d) Ru/C and (e, f) $Ru/Ni/Ni(OH)_2/C$ samples.

3. XRD patterns for the samples

Fig. S2 shows the XRD patterns for the $Ni/Ni(OH)_2/C$, $Ru/Ni/Ni(OH)_2/C$ and Ru/C catalysts. The two broad diffraction peaks at approximately 25° and 42° are related to carbon (002) and carbon (100),[8–10] respectively. As displayed in Fig. S2(a)

($Ni/Ni(OH)_2/C$), the characteristic diffraction peaks of $Ni(OH)_2(100)$, $Ni(OH)_2(101)$ and $Ni(OH)_2(110)$ planes can be observed at 2θ = 33.1°, 38.1° and 59.3° (JCPDS card No. 04-0117), respectively. And the diffraction peak at 2θ = 43.3° could be attributed to Ni(111) facets (JCPDS card No. 04-0850). It indicates that the crystalline Ni and $Ni(OH)_2$ phase co-existed in the $Ni/Ni(OH)_2$ sample. In Fig. S2(b), only two broad diffraction peaks corresponding to carbon(002) and Ni(111) planes can be seen, suggesting metal nanoparticles in $Ru/Ni/Ni(OH)_2/C$ are either very small or amorphous, with high dispersion. The diffraction peaks located at 2θ = 38.6°, 42.3° and 44.1° (Fig. S2(c)) can be identified for (100), (002) and (101) planes of hcp Ru crystalline structure, respectively (JCPDS card No. 06-0663).

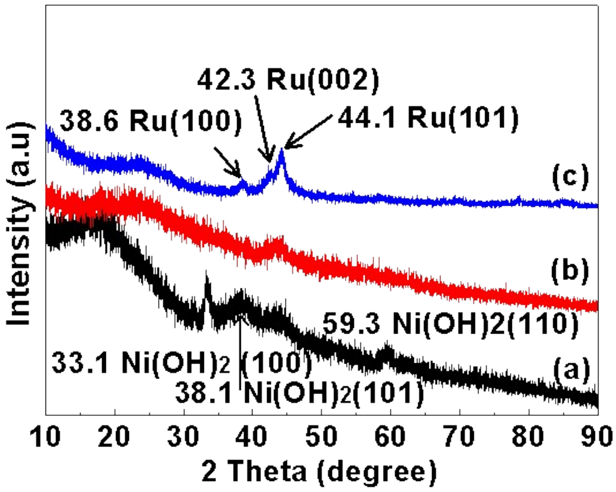

Fig. S2. X-ray diffraction (XRD) patterns for the samples. (a) $Ni/Ni(OH)_2/C$, (b) $Ru/Ni/Ni(OH)_2/C$ and (c) Ru/C. These XRD patterns results are the raw data, without any treatment (such as background subtraction and smoothing).

4. XPS spectra for the samples

To study the chemical states and surface composition of Ru and Ni species in $Ni/Ni(OH)_2/C$, $Ru/Ni/Ni(OH)_2/C$ and Ru/C, X-ray photoelectron spectroscopy (XPS) measurements were carried out, and the results are shown in Fig. S3. The binding energy of 852.7, 853.9, 855.4 and 857.1 eV in Ni $2p_{3/2}$ lines are assigned to Ni(0), NiO, $Ni(OH)_2$ and NiOOH species, respectively. The peaks at the binding energy of 870, 871.2, 872.9 and 874.4 eV in Ni $2p_{1/2}$ XPS spectra are attributed to Ni(0), NiO, $Ni(OH)_2$ and NiOOH, respectively (Fig. S3a, b).[11–14] The surface composition of different Ni species are listed in Table S2, indicating that the main Ni species in the Ni/$Ni(OH)_2$ and Ru/Ni/$Ni(OH)_2$/C samples are $Ni(OH)_2$ and NiOOH. The presence of NiOOH could be due to further oxidation of $Ni(OH)_2$ in air. Ru 3p XPS spectra for the Ru/C and Ru/Ni/$Ni(OH)_2$/C catalysts are shown in Fig. S3c, d. The peaks appearing at 462 eV and 464.2 eV represent Ru(0) and Ru^{4+} (RuO_2) specie, respectively. The other two peaks at higher binding energy (484 eV and 486.2 eV) are assigned to metallic ruthenium and oxidized state ruthenium (RuO_2), respectively.[15–17] The content of Ru(0) and RuO_2 on the surface of the catalyst are listed in Table S3. The existence of RuO_2 could be resulted from the surface oxidation of Ru(0) nanoclusters after the catalyst exposed to air for a long time.[18] Additionally, it can be obviously found that the RuO_2/Ru ratio on the surface of Ru/Ni/$Ni(OH)_2$/C is much larger than that on the surface of Ru/C. The possible reason is that Ru particles in Ru/Ni/$Ni(OH)_2$/C is smaller and displays better dispersion than those in Ru/C, resulting in Ru particles being more easily oxidized in air. Moreover, the binding energy of Ni(0) or Ru(0) specie in Ru/Ni/$Ni(OH)_2$/C is without any shift relative to the monometallic Ru-based and Ni-based catalysts,[19] indicating no Ru-Ni alloy forming. The above XPS results demonstrate that Ru and Ni element are present with two segregated phases in the Ru/Ni/$Ni(OH)_2$/C catalyst.

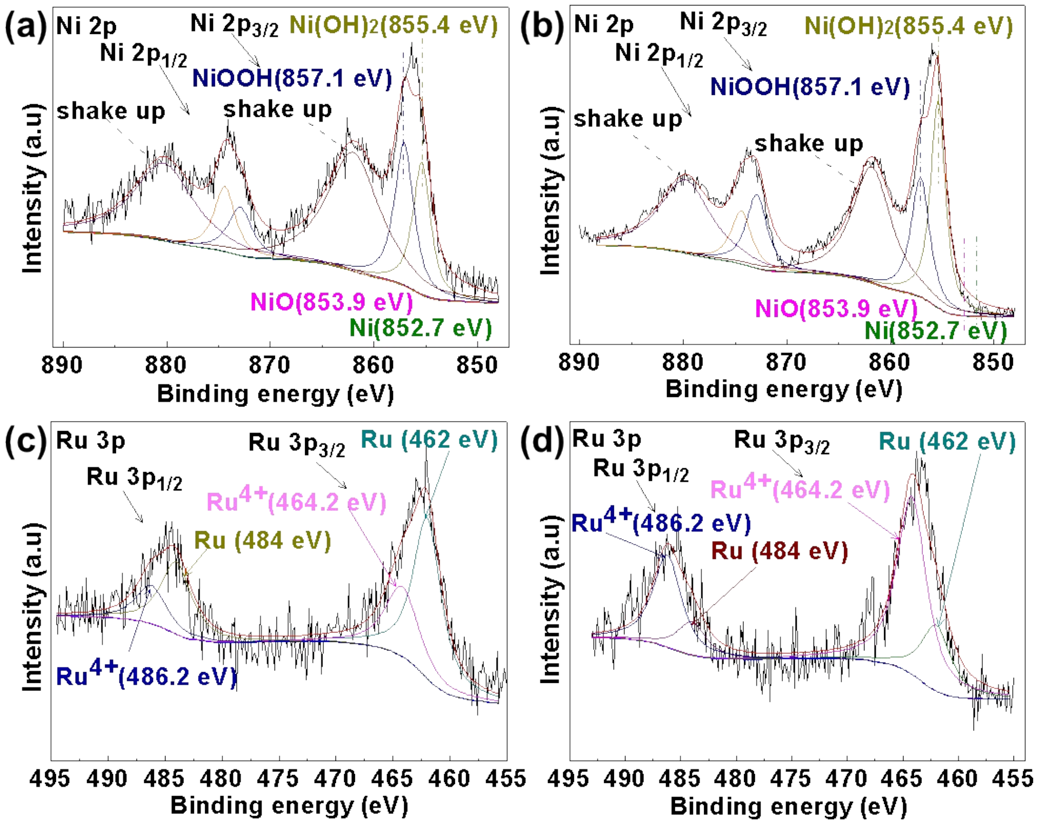

Fig. S3. XPS spectrum for the catalysts. Ni 2p spectrum for (a) Ni/Ni$(OH)_2$/C and (b) Ru/Ni/Ni$(OH)_2$/C; Ru 3p spectrum for (c) Ru/C and (d) Ru/Ni/Ni$(OH)_2$/C.

Table S2: Chemical states, binding energies (BE) and ratios of integrated intensities (atomic ratios; AR) of Ni element in the catalysts.

Catalysts		Ni $(2p_{3/2})$			
		Ni(0)	NiO	Ni$(OH)_2$	NiOOH
Ni/Ni$(OH)_2$/C	BE (eV)	852.7	853.9	855.4	857.1
	AR (%)	2.4	1.1	56.2	40.3
Ru/Ni/Ni$(OH)_2$/C	BE (eV)	852.7	853.9	855.4	857.1
	AR (%)	1.6	2.0	44.4	52.0

Table S3: Chemical states binding energies (BE) and ratios of integrated intensities (atomic ratios; AR) of Ru element in the catalysts.

Catalysts		Ru ($3p_{3/2}$)	
		Ru(0)	RuO_2
Ru/C	BE (eV)	462	464.2
	AR (%)	65.5	34.5
Ru/Ni/Ni(OH)$_2$/C	BE (eV)	462	464.2
	AR (%)	27.1	72.9

5. TEM and HRTEM images for the Ru/Ni/Ni(OH)$_2$/C catalyst

TEM and HRTEM images for Ru/Ni/Ni(OH)$_2$/C are displayed in Fig. S4.

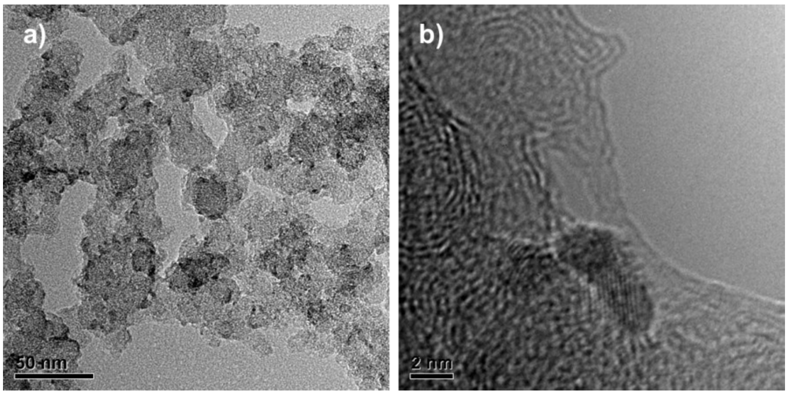

Fig. S4. a) TEM and b) HRTEM images for recycled Ru/Ni/Ni(OH)$_2$/C sample. .

6. HAADF-STEM image and elemental analysis for the Ru/Ni/Ni(OH)$_2$/C catalyst

High angle annular dark field-scanning transmission electron microscopy (HAADF-STEM) images for the Ru/Ni/Ni(OH)$_2$/C catalyst and energy dispersive X-ray spectroscopy (EDS) results are shown in Fig. S5. Many isolated bright nanoparticles can be clearly seen in Fig. S5a, demonstrating NPs containing heavier elements dispersed on carbon black. The EDS-mapping of Ni and Ru element are displayed in Fig. S5b, c, indicating that the co-existence of Ni and Ru species in the same nanoparticle. But for some of nanoparticles, the intensity of Ru element is larger than that of Ni element. Additionally, the distribution region of Ni element is found to deviate slightly from that of Ru element, suggesting the presence of isolated Ru-rich particles adjacent to those Ni-rich ones. The presence of Ru, Ni, C and O element was examined from the bright NPs on carbon by EDS, as shown in Fig. S5d. It is difficult to quantify the composition of Ru and Ni in the NPs due to the low EDS counts.

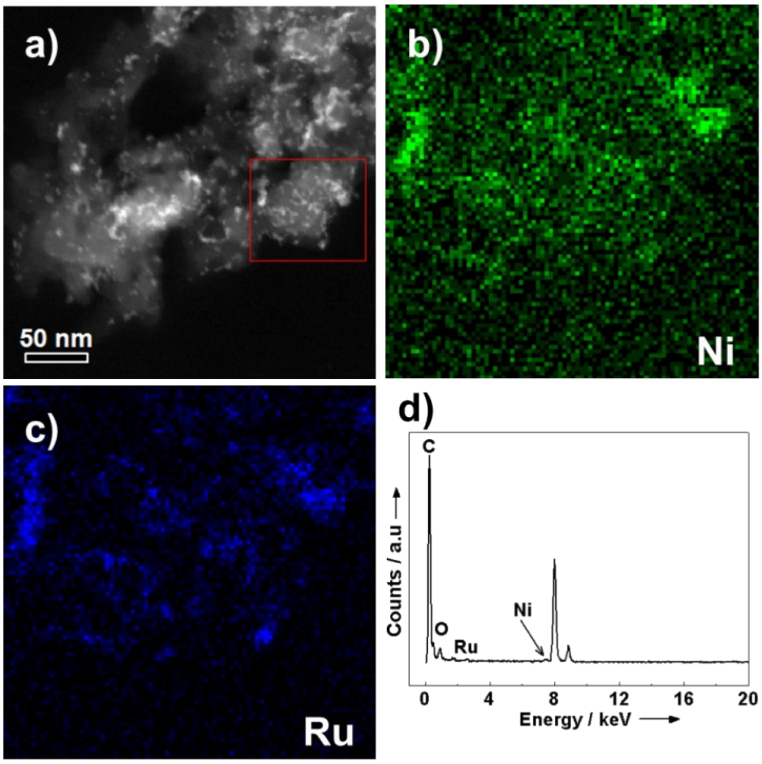

Fig. S5. a) HAADF-STEM image for the Ru/Ni/Ni(OH)$_2$/C sample, and EDS mapping of b) Ni (green) and c) Ru (blue) from the selected region, and d) EDS analysis results of the Ru/Ni/Ni(OH)$_2$/C sample.

In order to further investigate the elemental distribution and nanostructure of the Ru/Ni/Ni(OH)$_2$/C catalyst, the EDS-elemental mapping measurement for it was performed over other Ru-Ni NPs (as shown in Fig. S6A). The EDS-elemental mapping is weak due to the small NPs, but Ru and Ni are together present in the same NP and the location region of Ru could not overlap that of Ni. It indicates that Ru and Ni element co-existed in the Ru-Ni NPs with phase segregation. Fig. S6B shows HAADF-STEM image and EDS line-scan results for the Ru/Ni/Ni(OH)$_2$/C sample. It can be obviously observed that the intensity of Ni element signal is much larger than that of

Ru element on the side of the Ru-Ni NP. The position of the largest intensity of Ni element is located at about 32 nm, but that of the largest intensity of Ru element is located at about 28 nm. It demonstrates that the center of Ru-rich region deviates from that of Ni-rich region. Combining with the XRD, XPS and HRTEM characterization results, it suggests that the particles composed of Ru element are coated on the particles composed of Ni element.

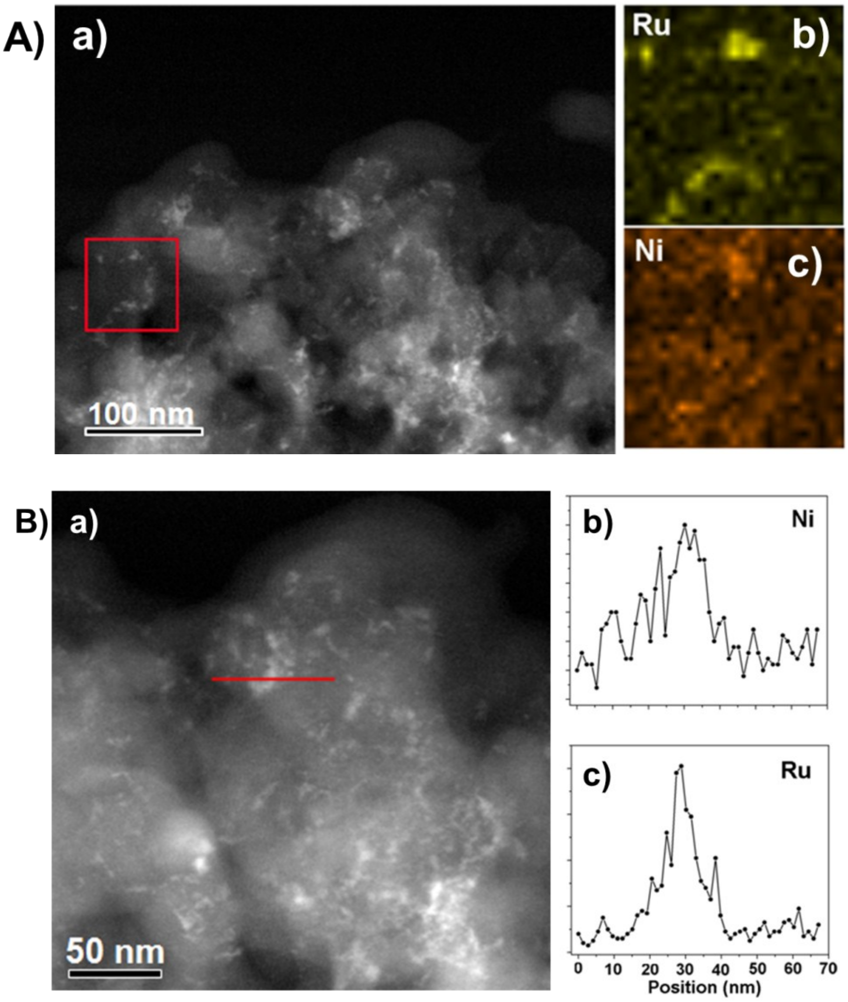

Fig. S6. A) a) HAADF-STEM image for the Ru/Ni/Ni(OH)$_2$/C sample, and EDS-elemental mapping of b) Ru (yellow) and c) Ni (orange) from the selected region; B) a) HAADF-STEM image for the Ru/Ni/Ni(OH)$_2$/C sample, and EDS line-scan results of individual Ru/Ni/Ni(OH)$_2$ NP along the arrow direction, b) Ni and c) Ru.

7. HE-XRD and atomic PDFs characterization results for the as-prepared catalyst

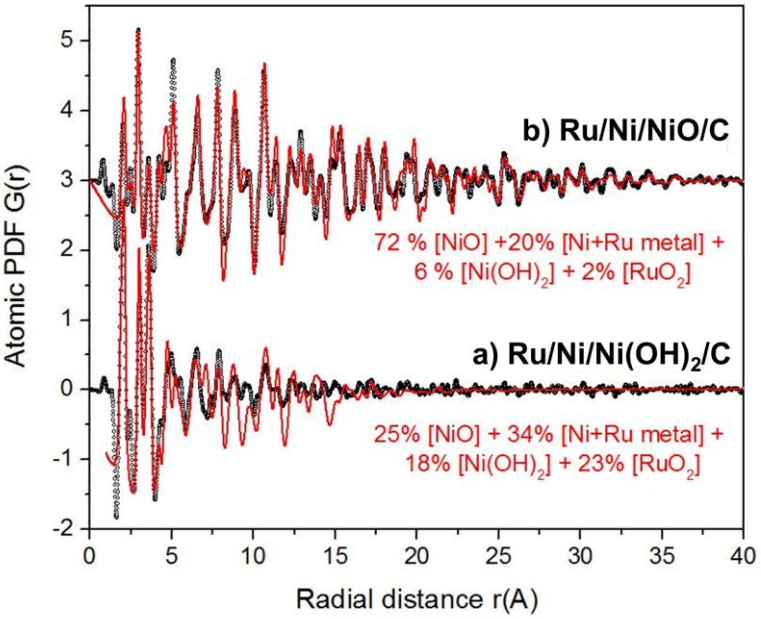

Fig. S7. Experimental (symbols) and computed (red line) atomic PDFs for the uncalcined and calcined catalyst. Computed PDFs are an weighted average of the PDFs characteristic to NiO, Ni and Ru metals, Ni(OH)$_2$ and RuO$_2$. The weights are given for each data set. Computations were done with the help of the program PDFgui.[20]

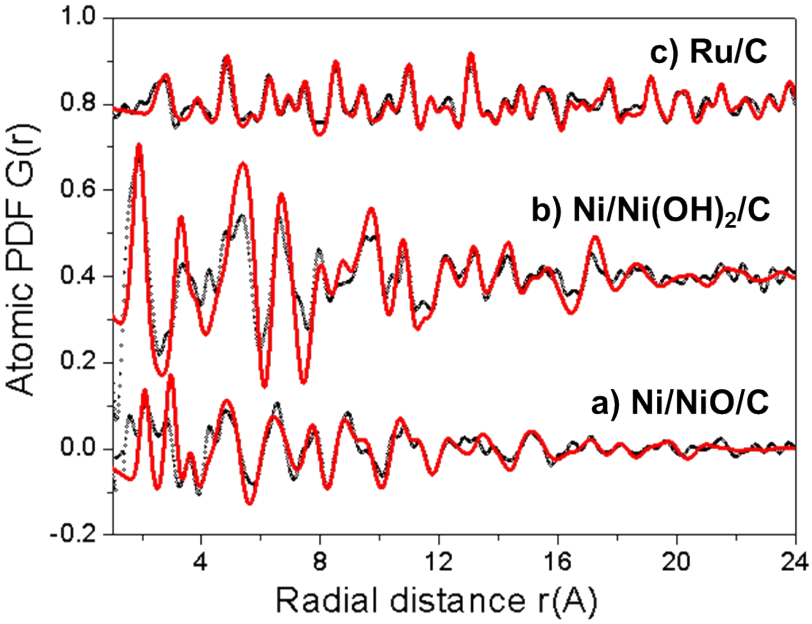

Fig. S8. Experimental (black symbols) and computed (red line) atomic PDFs for pure a) Ru/C, b) Ni/Ni(OH)$_2$/C and c) Ni/NiO/C standards. The standards were used in the phase analysis of the Ru/Ni/Ni(OH)$_2$/C and Ru/Ni/NiO/C catalyst. Results of the analysis are shown in the above Fig. S7.

8. EXAFS parameters of the samples

The best-fit EXAFS parameters of the samples are listed in Table S4, where the curve-fitting was conducted in R-space with the fitting range (R) and the R-factor (R_f) of fit indicated in the table. The amplitude fitting parameter for Ru *K*-edge was set to 0.80 and 0.93 for Ni *K*-edge XAS data. This value was refined from the Ru and Ni *K*-edge EXAFS analysis of the Ru and Ni foil, respectively, fixing the metal-metal coordination number. The coordination number (CN), neighbour shell radii (r) and Debye-Waller factor (σ^2) are calculated for each material based on the crystallographic radial distribution function of RuO_2 and RuNi alloy from the crystallographic database.

Notes and references

1 I. S. Park, M. S. Kwon, N. Kim, J. S. Lee, K. Y. Kang and J. Park, *Chem. Commun.*, 2005, 5667–5669.

2 A. D. Schmitz, G. Bowers and C. Song, *Catal. Today*, 1996, **31**, 45–56.

3 S. Ren, P. Zhang, H. Shui, Z. Lei, Z. Wang and S. Kang, *Catal. Commun*, 2010, **12**, 132–136.

4 T. Tang, C. Yin, L. Wang, Y. Ji and F. S. Xiao, *J. Catal.*, 2008, **257**, 125–133.

5 N. Hiyoshi, A. Yamaguchi, C. V. Rode, O. Sato and M. Shirai, *Catal. Commun.*, 2009, **10**, 1681–1684.

6 P. Zhang, T. Wu, M. Hou, J. Ma, H. Liu, T. Jiang, W. Wang, C. Wu and B. Han, *ChemCatChem,* 2014, **6**, 3323–3327.

7 S. R. Kirumakki, B. G. Shpeizer, G. V. Sagar, K. V. R. Chary and A. Clearfield, *J. Catal.*, 2006, **242**, 319–331.

8 U. G. Hong, J. K. Kim, J. Lee, J. K. Lee, J. H. Song, J. Yi and I. K. Song, *Appl. Catal., A*, 2014, **469**, 466–471.

9 M. Endo, Y. A. Kim, T. Takeda, S. H. Hong, T. Matusita, T. Hayashi and M. S. Dresselhaus, *Carbon*, 2001, **39**, 2003–2010.

10 H.-B. Zhang, G.-D. Lin, Z.-H. Zhou, X. Dong and T. Chen, *Carbon*, 2002, **40**, 2429–2436.

11 N. C. Barnard, S. G. R. Brown, F. Devred, J. W. Bakker, B. E. Nieuwenhuys and N. J. Adkins, *J. Catal.*, 2011, **281**, 300–308.

12 K.-W. Park, J.-H. Choi, B.-K. Kwon, S.-A. Lee, Y.-E. Sung, H.-Y. Ha, S.-A. Hong, H. Kim and A. Wieckowski, *J. Phys. Chem. B*, 2002, **106**, 1869–1877.

13 Y. Goto, K. Taniguchi, T. Omata, S. Otsuka-Yao-Matsuo, N. Ohashi, S. Ueda, H. Yoshikawa, Y. Yamashita, H. Oohashi and K. Kobayashi, *Chem. Mater.*, 2008, **20**, 4156–4160.

14 S. Sarkar, A. K. Sinha, M. Pradhan, M. Basu, Y. Negishi and T. Pal, *J. Phys. Chem. C*, 2011, **115**, 1659–1673.

15 N. Chakroune, G. Viau, S. Ammar, L. Poul, D. Veautier, M. M. Chehimi, C. Mangeney, F. Villain and F. Fiévet, *Langmuir*, 2005, **21**, 6788–6796.

16 Y. Yamauchi, T. Ohsuna and K. Kuroda, *Chem. Mater.*, 2007, **19**, 1335–1342.

17 K. Lasch, L. Jörissen and J. Garche, *J. Power Sources*, 1999, **84**, 225–230.

18 S. Miao, Z. Liu, B. Han, J. Huang, Z. Sun, J. Zhang and T. Jiang, *Angew. Chem., Int. Ed.*, 2006, **45**, 266–269.

19 L. Zhu, M. Cao, L. Li, Y. Tang, N. Zhang, J. Zheng, H. Zhou, Y. Li, L. Yang, C.-J. Zhong and B. H. Chen, *ChemCatChem*, 2014, **6**, 2039–2046.

20 C. L. Farrow, P. Juhas, J. W. Liu, D. Bryndin, E. S, Božin, J. Bloch, T. Proffen and S. J. L. Billinge, *J. Phys.: Condens. Matter.*, 2007, **19**, 335219.